

LEGNet: Lightweight Edge-Gaussian Driven Network for Low-Quality Remote Sensing Image Object Detection

Wei Lu, Si-Bao Chen*, Hui-Dong Li, Qing-Ling Shu, Chris H. Q. Ding, Jin Tang, and Bin Luo

Abstract—Remote sensing object detection (RSOD) faces formidable challenges in complex visual environments. Aerial and satellite images inherently suffer from limitations such as low spatial resolution, sensor noise, blurred objects, low-light degradation, and partial occlusions. These degradation factors collectively compromise the feature discriminability in detection models, resulting in three key issues: (1) reduced contrast that hampers foreground-background separation, (2) structural discontinuities in edge representations, and (3) ambiguous feature responses caused by variations in illumination. These collectively weaken model robustness and deployment feasibility. To address these challenges, we propose LEGNet, a lightweight network that incorporates a novel edge-Gaussian aggregation (EGA) module specifically designed for low-quality remote sensing images. Our key innovation lies in the synergistic integration of Scharr operator-based edge priors with uncertainty-aware Gaussian modeling: (a) The orientation-aware Scharr filters preserve high-frequency edge details with rotational invariance; (b) The uncertainty-aware Gaussian layers probabilistically refine low-confidence features through variance estimation. This design enables precision enhancement while maintaining architectural simplicity. Comprehensive evaluations across four RSOD benchmarks (DOTA-v1.0, v1.5, DIOR-R, FAIRIM-v1.0) and a UAV-view dataset (VisDrone2019) demonstrate significant improvements. LEGNet achieves state-of-the-art performance across five benchmark datasets while ensuring computational efficiency, making it well-suited for deployment on resource-constrained edge devices in real-world remote sensing applications. The code is available at <https://github.com/lwCVer/LEGNet>.

Index Terms—Object detection, remote sensing, UAV, low-quality images, feature extraction.

I. INTRODUCTION

REMOTE sensing object detection (RSOD) occupies a critical and challenging frontier in computer vision. In recent years, it has garnered increasing attention due to its unique complexities and broad range of applications. Unlike conventional object detection, which primarily focuses on ground-level images, RSOD deals with satellite or aerial imagery. These images are inherently affected by numerous factors that pose significant challenges. For instance, camera resolution variations can cause detail inconsistencies, where some regions appear sharp while others remain blurred. The altitude at which images are captured influences object

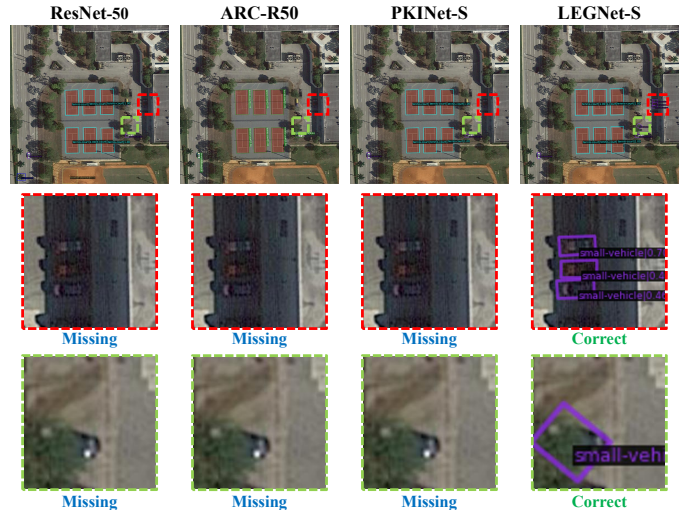


Fig. 1: Visualization results on DOTA-v1.0 test set [1]. All models were built with Oriented R-CNN [2]. Our LEGNet demonstrates robust detection under occlusion and low-light conditions, such as targets obscured by trees and buildings, surpassing previous state-of-the-art in accuracy and robustness.

scales, resulting in significant size variations for the same object across different images. Viewing angles play a crucial role—oblique perspectives can distort object shapes and sizes, complicating accurate recognition. Shadows cast by sunlight on buildings may reduce the contrast between the obscured objects and the background, lowering detection success rates. Occlusions from buildings or vegetation can obscure object features, increasing detection difficulty. These combined factors often lead to significant variations in object proportions and deterioration of image quality.

These challenges render the direct application of conventional object detection techniques inefficient. Traditional methods are primarily designed for ground-level images and lack the capability to extract features tailored to the unique characteristics of remote sensing (RS) imagery. This limitation underscores the urgent need for specialized algorithms and architectures capable of efficiently capturing multi-scale features and extracting low-quality object characteristics.

To address the persistent challenge of multi-scale detection in RSOD, numerous innovative approaches have been proposed. For instance, LSKNet [3] introduces large kernel convolutions to dynamically expand the receptive field, enabling the model to capture broader contextual information. This significantly enhances the model’s ability to perceive objects within diverse contexts. Additionally, PKINet [4] employs multi-scale convolutional kernels to extract features at varying

Corresponding author (*): Si-Bao Chen.

Wei Lu, Si-Bao Chen, Hui-Dong Li, Qing-Ling Shu, Jin Tang, and Bin Luo are with the MOE Key Laboratory of ICSP, IMIS Laboratory of Anhui, Anhui Provincial Key Laboratory of Multimodal Cognitive Computation, Zenmorn-AHU AI Joint Laboratory, School of Computer Science and Technology, Anhui University, Hefei 230601, China (e-mail: 2858191255@qq.com; sbchen@ahu.edu.cn; e23301341@stu.ahu.edu.cn; 2563489133@qq.com; tangjin@ahu.edu.cn; luobin@ahu.edu.cn).

Chris H. Q. Ding is with the School of Data Science (SDS), Chinese University of Hong Kong, Shenzhen 518172, China (e-mail: chrisding@cuhk.edu.cn).

spatial scales, effectively improving detection capabilities on multi-scale objects. While these methods have led to notable advancements in multi-scale detection, they, along with many others in the field, struggle to effectively represent low-quality or blurred objects—a prevalent issue in RS imagery, where degraded object features remain a pressing challenge.

RS images frequently suffer from inherent feature degradation. As features propagate through deep neural networks, they often become increasingly blurred or attenuated. This degradation profoundly impacts detection accuracy, making it difficult to reliably distinguish and identify objects, particularly in cases where features are indistinct or incomplete. For example, in shadowed or occluded regions with complex backgrounds, object features may be obscured or difficult to discern. Overcoming this limitation is crucial for achieving robust and precise RSOD.

To address the challenge of extracting features from low-quality objects in RS imagery, we introduce the lightweight edge-Gaussian network (LEGNet), a compact yet effective backbone network specifically designed for RSOD tasks. LEGNet integrates a novel edge-Gaussian aggregation (EGA) module, which leverages edge information and Gaussian modeling to enhance the representation of low-quality features. As illustrated in Fig. 1, LEGNet demonstrates strong robustness in detecting low-quality objects even under challenging conditions such as occlusions and low-light environments. For instance, it can effectively identify objects obscured by trees and shadows, which is significantly better than the previous state-of-the-art (SOTA) methods.

The LEG module is composed of two principal components: an edge-aware mechanism and a Gaussian-based feature representation module. The former employs boundary-sensitive feature extraction via Sobel operators to augment the precision of object boundary delineation, thereby offering substantial operational advantages in detecting targets within suboptimal imaging conditions characterized by low signal-to-noise ratios or motion-induced blur artifacts. Concurrently, the latter implements Gaussian-based uncertainty quantification through parameter-fixed convolution kernels, formally modeling the stochastic nature of feature representation while synergistically enhancing noise attenuation capabilities and foreground feature saliency. EGA module bridges the traditional image processing and modern deep learning paradigms. This dual-pronged methodological innovation—synergistically coupling spatial boundary refinement with uncertainty management in feature space—establishes a theoretically grounded framework essential for achieving robust RSOD performance under challenging environments, particularly when processing degraded RS visual data with inherent ambiguities and information loss.

To evaluate LEGNet’s performance, we conducted extensive experiments on four benchmark RSOD datasets as well as an additional UAV-view dataset. LEGNet outperforms existing methods with fewer parameters, achieving SOTA results. Specifically, it attains an mAP of 80.03% on DOTA-v1.0, 72.89% on DOTA-v1.5, 48.35% on FAIR1M-v1.0, 68.40% on DIOR-R, and 55.0% mAP50 on VisDrone2019. These results strongly validate the effectiveness of LEGNet in addressing the unique challenges of RSOD, particularly low-quality objects.

The main contributions are summarized as follows:

- We introduce a novel EGA module that theoretically bridges the traditional image processing and modern deep learning paradigms, significantly enhancing object boundary delineation and uncertainty management in RS imagery, and providing a novel approach to handle complex and low-quality features.
- We propose LEGNet, a lightweight backbone network designed specifically for RSOD, improving the representation of low-quality features in RS images.
- Comprehensive evaluations on multiple RSOD benchmark datasets demonstrate the superior performance of LEGNet, achieving SOTA results and providing a promising solution for low-quality feature extraction and representation in RSOD.

The manuscript is organized as follows. Section I introduces the challenges associated with RSOD tasks and presents the novel solutions proposed by LEGNet. Section II provides a comprehensive review of prior RSOD approaches. Section III details the architecture of LEGNet, focusing on the innovative EGA module. Section IV evaluates LEGNet’s performance on both RS and UAV-view object detection datasets, including extensive ablation studies. Section V summarizes the key findings and discusses potential directions for future research.

II. RELATED WORK

In recent years, deep learning and advanced feature representation techniques have significantly improved object detection performance. However, RSOD faces unique challenges, including significant scale variability, high object density, arbitrary orientations, and degraded feature quality due to sensor limitations and environmental factors, which complicate accurate detection in aerial and satellite imagery.

Traditional horizontal bounding box (HBB) methods, while effective for natural images, often struggle with remote sensing images due to their inability to accommodate arbitrarily oriented objects, leading to issues such as increased noise, overlapping detections, and reduced training efficiency. Consequently, oriented bounding box (OBB) approaches have emerged as the preferred solution for precise localization, addressing the limitations of HBBs in RS scenarios.

Early works, such as those by Yang et al. [5] and Azimi et al. [6], proposed rotated anchors with diverse scales, aspect ratios, and angles to enhance object coverage. While effective, these methods were computationally intensive and generated numerous negative samples, slowing convergence. Subsequent advancements, such as RoI Transformer [7], focused on generating oriented proposals to better handle arbitrary orientations. S²ANet [8] and R³Det [9] employed feature alignment techniques to boost precision, though boundary-related challenges persisted. Gliding Vertex [10] refined HBB corners using a sliding vertex strategy for improved orientation estimation, but reliance on horizontal regions of interest (RoIs) sometimes caused misalignment. Oriented RepPoints [11] adopted adaptive points for flexible RSOD modeling, offering a novel representation approach.

Optimizing loss functions for OBB regression has been crucial for enhancing model robustness. CSL [12] reframed

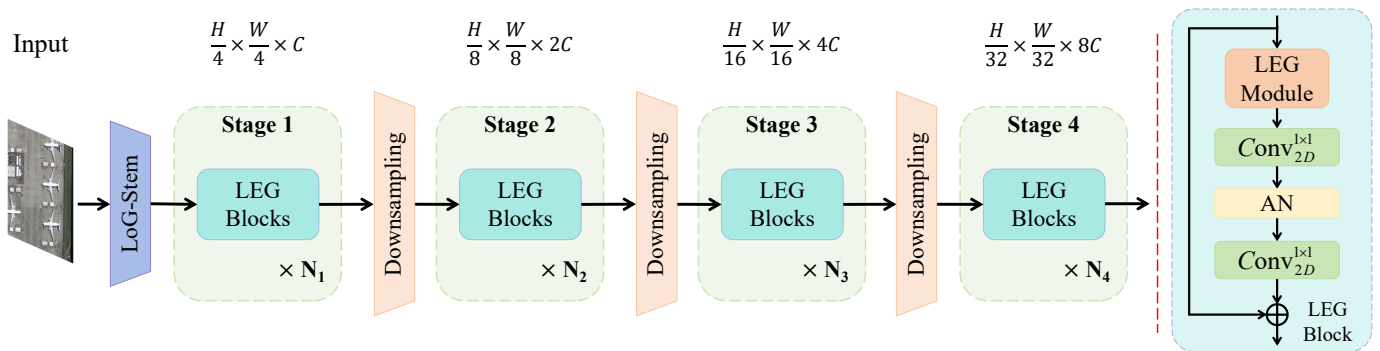


Fig. 2: Overview of LEGNet architecture. It encompasses four stages. H , W and C denote the feature height, width, and channel width, respectively. AN and Conv denote the norm layer with an activation function and convolutional layer, respectively.

angle regression as a classification task to address angular periodicity, while SCRDet [13] used an IoU-smooth L1 loss to mitigate angle discontinuity. Methods like GWD [14] and KLD [15] approximated skewed IoU using Gaussian measures, and KFIOU [16] leveraged Gaussian distributions and Kalman filtering for improved efficiency, providing continuous and differentiable loss functions for optimization.

Transformer-based methods have shown significant potential in RSOD. AO2-DETR [17] includes an oriented proposal generation mechanism, providing better position priors for pooling features modulated through the Transformer decoder’s cross-attention. FPNformer [18] integrates feature pyramid network (FPN) for multi-scale feature extraction with the Transformer decoder for scale- and angle-aware feature fusion, enhancing detection accuracy by capturing long-range dependencies.

The choice of backbone network is critical for effective feature representation in RSOD. ARC [19] applies adaptive rotation in convolutional kernels to enhance orientation recognition, while LSKNet [3] dynamically adjusts receptive fields to capture contextual information. PKINet [4] uses multi-scale convolutional kernels to improve local context capture for robust detection across varied object scales. DecoupleNet [20] incorporates a feature integration downsampling module to preserve small object features and a multi-branch feature decoupling module for multi-scale RS object extraction, achieving a balance between lightness and accuracy. LWGANet [21] utilizes multi-scale feature extraction, achieving excellent performance in multiple RS visual tasks.

To address degraded feature quality in low-quality RS images, recent research has focused on super-resolution techniques [22], [23] to enhance image resolution, improving visibility of small or distant objects, and generative adversarial networks (GANs) [24], [25] to generate or refine images, reducing noise and enhancing specific features. Methods incorporating edge information and Gaussian models, such as [26], robustly handle noise and variability by representing objects with Gaussian distributions, capturing uncertainty and orientation effectively.

These advancements underscore ongoing efforts to tackle RSOD challenges in low-quality images. Building on this, we propose LEGNet, a lightweight, edge-Gaussian-driven network designed to enhance feature extraction from low-quality RS images. LEGNet leverages edge information to capture

fine details and boundaries, often obscured in low-quality images, and Gaussian-guided modeling to handle uncertainty and variability in object shapes and orientations, achieving SOTA performance with computational efficiency.

III. METHOD

This section presents the architecture and key components of the proposed LEGNet network, designed to tackle the challenges of RSOD in low-quality images by leveraging edge details and Gaussian modeling information.

A. LEGNet Architecture Overview

As shown in Figure 2, LEGNet is a multi-stage architecture that progressively extracts multi-scale features with downsampling ratios of 1/4, 1/8, 1/16, and 1/32 for Stages 1-4, respectively. It consists of three main components: a LoG-stem layer, downsampling modules using the deep robust feature downsampling (DRFD) method, and lightweight edge-Gaussian (LEG) blocks.

The input image $\mathbf{I} \in \mathbb{R}^{H \times W \times 3}$ is first passed through the LoG-stem layer, which uses a Laplacian of Gaussian (LoG) filter to perform initial downsampling and capture edge information. This produces a feature map $\mathbf{F}_{\text{stem}} \in \mathbb{R}^{\frac{H}{4} \times \frac{W}{4} \times C}$, where C is 32 for LEGNet Tiny and 64 for LEGNet Small.

Following the LoG-stem layer, stage 1 consists of N_1 LEG blocks that process \mathbf{F}_{stem} to refine features at the 1/4 downsampling rate. Each LEG block integrates edge detection and Gaussian modeling to enhance the network’s robustness to noise and variability in object shapes and orientations.

For Stages 2-4, each stage begins with a DRFD module [27], which combines convolutional and max-pooling downsampling to retain essential small-scale features while reducing spatial dimensions. This is followed by N_2 , N_3 , and N_4 LEG blocks, respectively, to further refine features at downsampling rates of 1/8, 1/16, and 1/32.

LEG blocks in each stage leverage edge information or Gaussian modeling to enhance feature representation, making the network particularly suited for low-quality images.

Finally, the outputs from all four stages are aggregated in the RSOD decoder to produce the detection results. Detailed configurations of LEGNet are provided in Table I.

TABLE I: Architecture configurations of LEGNet.

Stage	Downs. Rate	Layer Specification	Input / Output channels (C)	
			Tiny	Small
1	$\frac{H}{4} \times \frac{W}{4}$	LoG-Stem Layer	3/32	3/64
		[LEG Block] $\times N_1$	32/32	64/64
2	$\frac{H}{8} \times \frac{W}{8}$	DRFD Module	32/64	64/128
		[LEG Block] $\times N_2$	64/64	128/128
3	$\frac{H}{16} \times \frac{W}{16}$	DRFD Module	64/128	128/256
		[LEG Block] $\times N_3$	128/128	256/256
4	$\frac{H}{32} \times \frac{W}{32}$	DRFD Module	128/256	256/512
		[LEG Block] $\times N_4$	256/256	512/512
Number of Block			$[N_1, N_2, N_3, N_4] = [1, 4, 4, 2]$	

B. LoG-Stem Layer

To address the inherent challenges posed by the low-quality of RS images, characterized by noise, variability, and degraded edge information, we introduce the Laplacian of Gaussian (LoG)-stem layer as a pioneering component in our network architecture. This layer is strategically designed to enhance edge features at the initial processing stage, leveraging the LoG filter’s dual capability of noise reduction and edge detection, which is particularly critical for RS images where traditional feature extraction methods often falter.

The LoG filter, a fusion of Gaussian smoothing and Laplacian sharpening, is renowned for its robustness in detecting edges in noisy environments. The Gaussian component mitigates noise, while the Laplacian operator highlights regions of rapid intensity change, making it an ideal choice for RS images with varying noise levels. In our implementation, the input image $\mathbf{I} \in \mathbb{R}^{H \times W \times 3}$ first undergoes a 7×7 convolutional transformation to extract initial features, followed by the application of the LoG filter with a kernel size of 7×7 and $\sigma = 1.0$. This sequence enables the network to learn feature representations and subsequently emphasize their edges, a novel integration of traditional image processing with deep learning paradigms.

The 2D LoG filter at position $\mathbf{x} = (x, y)$ is defined as:

$$\text{LoG}_{\sigma}^{k \times k}(\mathbf{x}) = \frac{1}{\pi\sigma^4} \left(1 - \frac{x^2 + y^2}{\sigma^2} \right) e^{-\frac{x^2 + y^2}{2\sigma^2}}, \quad (1)$$

where the Gaussian filter $G_{\sigma}^{k \times k}(\mathbf{x})$ is given by:

$$G_{\sigma}^{k \times k}(\mathbf{x}) = \frac{1}{2\pi\sigma^2} e^{-\frac{x^2 + y^2}{2\sigma^2}}. \quad (2)$$

Here, $k \times k$ denotes the kernel size, and σ is the standard deviation, set to 1.0 in our case for optimal edge detection.

The processed features are enhanced through a residual connection in which the output of the LoG filter is first passed through an activation function and batch normalization (AN), and then combined with the original image \mathbf{I} :

$$\mathbf{F}_{LoG} = \text{Norm}(\mathbf{I} + \text{AN}(\text{LoG}_{1.0}^{7 \times 7}(\text{Conv}_{2D}^{7 \times 7}(\mathbf{I})))) .$$

The residual-like structure ensures smooth gradient flow and preserves original image details and edge information, which is crucial for maintaining robustness against noise and variability in low-quality images.

Subsequently, \mathbf{F}_{LoG} is processed through two convolutional layers: a standard 3×3 convolution followed by a 3×3 convolution with stride 2 for downsampling, producing \mathbf{F}_1 :

$$\mathbf{F}_1 = \text{ConvD}_{2D}^{3 \times 3}(\text{Conv}_{2D}^{3 \times 3}(\mathbf{F}_{LoG})) .$$

This step reduces the spatial dimensions to $\frac{H}{2} \times \frac{W}{2}$, facilitating efficient feature extraction.

To further refine the feature map and integrate multi-scale uncertainty information, \mathbf{F}_1 is processed through two Gaussian filters of different sizes (9×9 and 5×5 with $\sigma = 0.5$), combined, normalized, and then downsampled using the DRFD module to achieve the final downsampling ratio of 1/4:

$$\mathbf{F}_{stem} = \text{DRFD}(G_{0.5}^{5 \times 5}(\text{Norm}(G_{0.5}^{9 \times 9}(\mathbf{F}_1) + \mathbf{F}_1))) .$$

The use of multiple Gaussian filters enables multi-scale uncertainty feature integration, enhancing the network’s capability to capture features at different resolutions, which is crucial for detecting objects of varying sizes in RS images.

The innovative LoG-stem layer enhances edge features and integrates multi-scale uncertainty information, providing a robust and efficient foundation for subsequent stages.

The output feature map $\mathbf{F}_{stem} \in \mathbb{R}^{\frac{H}{4} \times \frac{W}{4} \times C}$ is then passed into the LEG blocks of Stage 1.

C. LEG Block

As depicted in Fig. 2, LEG block processes \mathbf{F}_{in} through EGA module to enhance low-quality feature robustness. Initially, \mathbf{F}_{in} is processed by LEG module to produce an enhanced feature map. This enhanced map is then passed through a 1×1 convolutional layer that doubles the number of channels from C to $2C$, followed by an AN layer to generate \mathbf{F}_{o1} :

$$\mathbf{F}_{o1} = \text{AN}(\text{Conv}_{2D}^{1 \times 1}(\text{LEG}(\mathbf{F}_{in}))) .$$

Subsequently, \mathbf{F}_{o1} is convolved again with a 1×1 kernel to reduce the channels back to C . The output of this convolution is then normalized and dropout is applied. Finally, this processed feature map is added to the original input \mathbf{F}_{in} to produce the output feature map \mathbf{F}_o . This residual-like structure ensures that the network can effectively learn low-quality features while preserving the integrity of the input features:

$$\mathbf{F}_o = \mathbf{F}_{in} + \text{Norm}(\text{drop}(\text{Conv}_{2D}^{1 \times 1}(\mathbf{F}_{o1}))) ,$$

where drop represents dropout with a rate of 0.1.

Given that low-quality RS images often suffer from issues such as noise and blur, LEG module is designed to enhance feature robustness by integrating edge extraction and Gaussian modeling mechanisms. This combination allows the network to capture precise edge details in early stages and focus on salient features in later stages, thereby improving the accuracy of object detection in challenging conditions.

1) *Edge Extraction*: In Stage 1, where the feature resolution is reduced to a quarter of the input size, the features retain rich edge details and high-frequency information crucial for object localization. To extract robust edge features from low-quality objects, we employ the Scharr filter, which is a refined version of the Sobel operator, providing superior rotation invariance

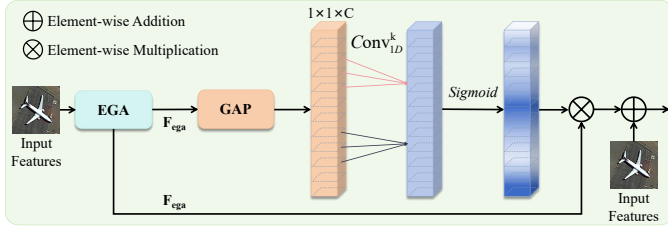


Fig. 3: Illustration of LEG module. GAP and k denote global average pooling and convolutional kernel size, respectively.

and minimizing edge response errors. The Scharr filters are defined as:

$$S_x = \begin{bmatrix} -3 & 0 & 3 \\ -10 & 0 & 10 \\ -3 & 0 & 3 \end{bmatrix}, \quad S_y = \begin{bmatrix} -3 & -10 & -3 \\ 0 & 0 & 0 \\ 3 & 10 & 3 \end{bmatrix}.$$

These filters are assigned separately to the parameters of $\text{Conv}_{2D}^{S_x}$ and $\text{Conv}_{2D}^{S_y}$ convolution layers, which process the input feature map \mathbf{F}_{in} in the horizontal and vertical directions, respectively. The edge responses from both directions are combined using the Euclidean norm to yield the final edge attention \mathbf{A}_{edge} :

$$\mathbf{A}_{edge} = \sqrt{(\text{Conv}_{2D}^{S_x}(\mathbf{F}_{in}))^2 + (\text{Conv}_{2D}^{S_y}(\mathbf{F}_{in}))^2},$$

where S_x and S_y denote the parameters of the respective convolution filters. This edge attention effectively enhances edge information before further processing.

2) *Gaussian Modeling*: In Stages 2-4, the ability to distinguish edge information diminishes as the feature dimension decreases. In contrast, the features of objects tend to follow a normal distribution centered around a particular point. To better capture these object features, Gaussian convolution kernels are employed, which help preserve the critical and uncertain features and prevent their degradation during the forward propagation of the network.

To enhance salient features, a fixed Gaussian kernel is used. As described in Eqn. (2), the Gaussian filter assigns higher weights to pixels closer to the center of the kernel, emphasizing prominent features in the image while suppressing background noise. This property makes the Gaussian filter particularly effective for enhancing salient features in feature maps, enabling the network to focus on the most informative regions while minimizing artifacts from high-frequency noise.

The Gaussian kernel is applied through depthwise convolution, which independently smooths the features in each channel. The Gaussian modeling \mathbf{A}_{gauss} is computed as:

$$\mathbf{A}_{gauss} = \mathbf{G}_{1.0}^{5 \times 5}(\mathbf{F}_{in}).$$

3) *LEG Module*: The LEG module, shown in Fig. 3, processes the input feature \mathbf{F}_{in} through an edge-Gaussian aggregation (EGA) submodule, which yield the features \mathbf{F}_{ega} . To emphasize critical channels, we adopt an efficient channel attention (ECA) strategy [28]. The ECA is represented as:

$$\begin{aligned} \mathbf{F}_{o1} &= \text{Sigmoid}(\text{Conv}_{1D}^k(\text{GAP}(\mathbf{F}_{ega}))), \\ \mathbf{F}_o &= \text{Norm}((\mathbf{F}_{o1} \otimes \mathbf{F}_{ega}) + \mathbf{F}_{in}), \end{aligned}$$

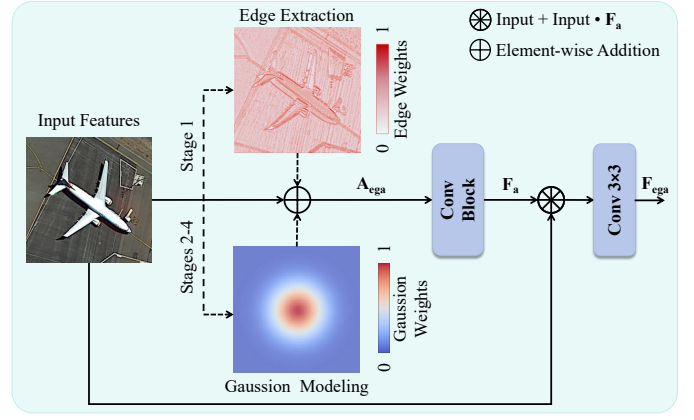


Fig. 4: Illustration of EGA module.

where Conv_{1D}^k is an adaptive one-dimensional convolution with kernel size k proportional to the channel count C , and GAP is channel-wise global average pooling. This strategy selectively enhances essential channels while minimizing redundant features, thus improving feature semantics.

4) *EGA Module*: As shown in Fig. 4, EGA module processes the input feature \mathbf{F}_{in} through a selection mechanism, which applies either edge extraction or Gaussian modeling depending on the stage:

$$\mathbf{A}_{ega} = \begin{cases} \mathbf{A}_{edge}(\mathbf{F}_{in}), & \text{if Stage} = 1, \\ \mathbf{A}_{gauss}(\mathbf{F}_{in}), & \text{otherwise.} \end{cases}$$

The result \mathbf{A}_{ega} is added to \mathbf{F}_{in} , and the sum is processed via a convolutional block (Conv_Block) to enhance feature representation, producing \mathbf{F}_a :

$$\mathbf{F}_a = \text{Conv_Block}(\mathbf{F}_{in} \oplus \mathbf{A}_{ega}),$$

where \oplus denotes element-wise addition, Conv_Block is a sequential processing unit defined as follows:

1. Apply a 1×1 convolution to adjust channel number.
2. Apply Activation and Normalization (AN).
3. Apply a 3×3 convolution to capture spatial relationships.
4. Apply another AN.
5. Apply a 1×1 convolution to adjust channels back.
6. Apply normalization.

Specifically, for an input \mathbf{X} , Conv_Block(\mathbf{X}) is defined as:

$$\mathbf{X}_1 = \text{Conv}_{2D}^{1 \times 1}(\mathbf{X}), \mathbf{X}_2 = \text{AN}(\mathbf{X}_1),$$

$$\mathbf{X}_3 = \text{Conv}_{2D}^{3 \times 3}(\mathbf{X}_2), \mathbf{X}_4 = \text{AN}(\mathbf{X}_3),$$

$$\mathbf{X}_5 = \text{Conv}_{2D}^{1 \times 1}(\mathbf{X}_4),$$

$$\text{Conv_Block}(\mathbf{X}) = \text{Norm}(\mathbf{X}_5).$$

In our case, $\mathbf{X} = \mathbf{F}_{in} \oplus \mathbf{A}_{ega}$, and the 1×1 convolutions handle channel resizing as needed.

Further refinement involves combining \mathbf{F}_{in} and \mathbf{F}_a using element-wise multiplication and addition operations, followed by a 3×3 convolution to yield the features \mathbf{F}_{ega} :

$$\mathbf{F}_{ega} = \text{Conv}_{2D}^{3 \times 3}((\mathbf{F}_{in} \otimes \mathbf{F}_a) + \mathbf{F}_{in}),$$

where \otimes indicates element-wise multiplication.

5) *Macro Design*: Through rigorous fine-tuning experiments, we have determined that edge information is optimally utilized when incorporated into the shallow layers of our network. The introduction of such information in deeper layers not only fails to enhance performance but also impedes the network’s capacity to learn complex, higher-order features, often resulting in suboptimal convergence or training difficulties.

To address this, for deep features, we employ a Gaussian modeling approach. By representing these features as Gaussian distributions, we effectively mitigate noise and capture the inherent uncertainty in their representations.

To harmonize the contributions from both the original input images and their corresponding edge components, we integrate extensive residual connections within LEG module. These connections facilitate an adaptive and dynamic adjustment of the network, allowing it to balance and combine these components effectively, thus alleviating any potential imbalance in their influence on the final feature representations. Additionally, a select few standard convolutional layers are employed to further refine and process these combined features.

To mitigate noise in RS images, we utilize the Gaussian component of the LoG operator in the shallow layers. This step is pivotal in suppressing noise interference, ensuring that the edge information extracted is of high quality and less corrupted by noise. In the deeper layers, the omission of explicit edge extraction mechanisms prevents the network from fixating on low-level features, thereby avoiding the issue of redundant edges and promoting the learning of more abstract, semantically meaningful representations.

In conclusion, LEG module combines edge extraction and Gaussian modeling to enhance low-quality feature robustness, enabling accurate detection in low-quality RS images.

IV. EXPERIMENTS

This section presents a comprehensive evaluation of the proposed LEGNet network on the RSOD task. We conducted extensive experiments on four RSOD benchmark datasets: DOTA-v1.0 [1], DOTA-v1.5 [1], DIOR-R [29], and FAIR1M-v1.0 [30] and a UAV-view benchmark dataset: VisDrone2019 [31]. The experimental results on the DOTA-v1.0, DOTA-v1.5, and FAIR1M-v1.0 datasets were obtained through online testing, ensuring fairness and reproducibility of the results. These datasets provided a diverse set of challenges, including variations in scale, object feature quality, fine-grained object detection, and the detection of small objects. The broad spectrum of complexities across these datasets offered an insightful evaluation of LEGNet’s robustness and performance in real-world RSOD scenarios.

A. Datasets

- **DOTA-v1.0** [1] was a widely recognized dataset for RSOD, consisting of 2,806 high-resolution images with 188,282 annotated instances. The dataset included 15 object categories, ranging from common objects like planes and bridges to rarer ones such as baseball diamonds, storage tanks, and helicopters. The images varied in terms of object sizes, orientations, and aspect ratios, making DOTA-v1.0 a

challenging benchmark for evaluating RSOD methods. It was divided into 1,411 training images, 458 validation images, and 937 test images.

- **DOTA-v1.5** [1] extended DOTA-v1.0 by adding a new category, container cranes (CC), and increasing the number of small objects (objects with fewer than 10 pixels). The dataset now included 403,318 instances, providing a more challenging scenario for detecting small, densely packed objects, which was crucial for evaluating the fine-grained performance of RSOD models.

- **FAIR1M-v1.0** [30] was one of the largest and most recent dataset for RSOD, containing 15,266 high-resolution images with over 1 million annotated instances. The dataset included 5 primary categories, subdivided into 37 sub-categories. This dataset was particularly valuable for testing models on fine-grained classification and detection, as it captured significant object variation and complexity. Its large scale and diversity set a new benchmark for RSOD tasks, especially in terms of scale and object variation.

- **DIOR-R** [29] was an extension of the DIOR dataset [32] that included OBB annotations for precise object localization. It contained 23,463 images with a resolution of 800×800 pixels and 192,518 annotated instances across various categories.

- **VisDrone2019** [31] is a large-scale benchmark for UAV-based vision tasks, comprising 2,580 images and video sequences captured by drone platforms across diverse scenarios and weather conditions, with manually annotated bounding boxes and attribute labels for multiple object categories (e.g., pedestrians and vehicles). Characterized by dense target distributions and complex background interference, it provides standardized training, validation, and test subsets to facilitate the development and evaluation of algorithms for object detection and multi-object tracking tasks.

B. Implementation Details

To ensure a fair comparison with previous SOTA methods [3], [4], [19], we pre-trained our backbone on ImageNet-1K [33] for 300 epochs, which helped improve the model’s robustness when applied to RSOD datasets. During pre-training, we employed the AdamW optimizer [34] with a momentum of 0.9 and weight decay of 0.05. We also adopted a cosine learning rate schedule [35] with a warm-up strategy to gradually adjust the learning rate.

For training RSOD models, we followed the training and testing configurations used in prior work for consistency. Specifically, for the DOTA-v1.0, DOTA-v1.5, and DIOR-R dataset, we employed a single-scale training and testing strategy with a $3 \times$ scale factor. The images from these datasets were cropped into 1024×1024 patches with 200-pixel overlaps for DOTA-v1.0 and DOTA-v1.5, and the input size was set to 800×800 for DIOR-R. For the FAIR1M-v1.0 dataset, we used a multi-scale training and testing strategy with a $1 \times$ scale factor, following the settings of the previous method [3], where images were rescaled to three scales (0.5, 1.0, 1.5) before cropping into 1024×1024 sub-images with 500-pixel overlaps. For the VisDrone2019 dataset, we employed a single-scale training and testing strategy with a $1 \times$ scale factor. The input size was set to 1333×800 .

TABLE II: Experimental results on DOTA-v1.0 test set [1] under single-scale training and testing setting. Other experimental results were referenced from [4], [20]. The red and blue indicated the best and second-best results for each column, respectively.

Method	Backbone	#P ↓	PL	BD	BR	GTF	SV	LV	SH	TC	BC	ST	SBF	RA	HA	SP	HC	mAP ↑	
<i>DETR-based</i>																			
AO2-DETR [17]	ResNet-50 [38]	40.8M	87.99	79.46	45.74	66.64	78.90	73.90	73.30	90.40	80.55	85.89	55.19	63.62	51.83	70.15	60.04	70.91	
O ² -DETR [39]	ResNet-50 [38]	-	86.01	75.92	46.02	66.65	79.70	79.93	89.17	90.44	81.19	76.00	56.91	62.45	64.22	65.80	58.96	72.15	
ARS-DETR [40]	ResNet-50 [38]	41.6M	86.61	77.26	48.84	66.76	78.38	78.96	87.40	90.61	82.76	82.19	54.02	62.61	72.64	72.80	64.96	73.79	
<i>One-stage</i>																			
R ³ Det [9]	ResNet-50 [38]	41.9M	89.00	75.60	46.64	67.09	76.18	73.40	79.02	90.88	78.62	84.88	59.00	61.16	63.65	62.39	37.94	69.70	
SASM [41]	ResNet-50 [38]	36.6M	86.42	78.97	52.47	69.84	77.30	75.99	86.72	90.89	82.63	85.66	60.13	68.25	73.98	72.22	62.37	74.92	
O-RepPoints [11]	ResNet-50 [38]	36.6M	87.02	83.17	54.13	71.16	80.18	78.40	87.28	90.90	85.97	86.25	59.90	70.49	73.53	72.27	58.97	75.97	
R ³ Det-GWD [14]	ResNet-50 [38]	41.9M	88.82	82.94	55.63	72.75	78.52	83.10	87.46	90.21	86.36	85.44	64.70	61.41	73.46	76.94	57.38	76.34	
R ³ Det-KLD [15]	ResNet-50 [38]	41.9M	88.90	84.17	55.80	69.35	78.72	84.08	87.00	89.75	84.32	85.73	64.74	61.80	76.62	78.49	70.89	77.36	
S ² ANet [8]	ResNet-50 [38]	38.5M	89.11	82.84	48.37	71.11	78.11	78.39	87.25	90.83	84.90	85.64	60.36	62.60	65.26	69.13	57.94	74.12	
	ARC-R50 [19]	71.8M	89.28	78.77	53.00	72.44	79.81	77.84	86.81	90.88	84.27	86.20	60.74	68.97	66.35	71.25	65.77	75.49	
	PKINet-S [4]	24.8M	89.67	84.16	51.94	71.89	80.81	83.47	88.29	90.80	87.01	86.94	65.02	69.53	75.83	80.20	61.85	77.83	
	LEGNet-S (Ours)	23.9M	89.22	85.04	55.59	75.73	81.42	84.56	88.32	90.90	87.90	87.02	65.98	70.13	77.56	81.88	69.26	79.37	
<i>Two-stage</i>																			
CenterMap [42]	ResNet-50 [38]	41.1M	89.02	80.56	49.41	61.98	77.99	74.19	83.74	89.44	78.01	83.52	47.64	65.93	63.68	67.07	61.59	71.59	
SCRDet [13]	ResNet-50 [38]	41.9M	89.98	80.65	52.09	68.36	68.36	60.32	72.41	90.85	87.94	86.86	65.02	66.68	66.25	68.24	65.21	72.61	
FR-O [43]	ResNet-50 [38]	41.1M	89.40	81.81	47.28	67.44	73.96	73.12	85.03	90.90	85.15	84.90	56.60	64.77	64.70	70.28	62.22	73.17	
Roi Trans. [7]	ResNet-50 [38]	55.1M	89.01	77.48	51.64	72.07	74.43	77.55	87.76	90.81	79.71	85.27	58.36	64.11	76.50	71.99	54.06	74.05	
G.V. [10]	ResNet-50 [38]	41.1M	89.64	85.00	52.26	77.34	73.01	73.14	86.82	90.74	79.02	86.81	59.55	70.91	72.94	70.86	57.32	75.02	
ReDet [44]	ResNet-50 [38]	31.6M	88.79	82.64	53.97	74.00	78.13	84.06	88.04	90.89	87.78	85.75	61.76	60.39	75.96	68.07	63.59	76.25	
O-RCNN [2]	ResNet-50 [38]	41.1M	89.46	82.12	54.78	70.86	78.93	83.00	88.20	90.90	87.50	84.68	63.97	67.69	74.94	68.84	52.28	75.87	
	ARC-R50 [19]	74.4M	89.40	82.48	55.33	73.88	79.37	84.05	88.06	90.90	86.44	84.83	63.63	70.32	74.29	71.91	65.43	77.35	
	LSKNet-S [3]	31.0M	89.66	85.52	57.72	75.70	74.95	78.69	88.24	90.88	86.79	86.38	66.92	63.77	77.77	74.47	64.82	77.49	
	DecoupleNet-D2 [20]	23.3M	89.37	83.25	54.29	75.51	79.83	84.82	88.49	90.89	87.19	86.23	66.07	65.53	77.23	72.34	69.62	78.04	
	PKINet-S [4]	30.8M	89.72	84.20	55.81	77.63	80.25	84.45	88.12	90.88	87.57	86.07	66.86	70.23	77.47	73.62	62.94	78.39	
	LEGNet-T (Ours)	20.6M	89.45	86.49	55.76	76.38	80.59	85.40	88.42	90.90	88.72	86.42	65.24	67.81	77.93	73.49	71.39	78.96	
LEGNet-S (Ours)	29.8M	89.87	86.32	56.36	78.67	81.34	85.29	88.53	90.89	87.31	86.46	70.38	68.48	78.34	82.00	70.25	80.03		

The AdamW optimizer [34] was used with a weight decay of 0.05 and an initial learning rate of 0.0002. We performed random resizing and flipping of images during training, as done in previous works [3], [4], [19], [20]. At the testing stage, we maintained the same resolution used during training to ensure consistency.

All experiments were conducted using the MMRotate framework [36] with PyTorch [37] on an Ubuntu 20.04 platform. We leveraged 4 NVIDIA RTX 3090 GPUs for both ImageNet-1K pre-training and RSOD training and testing. Unless specified otherwise, LEGNet was integrated within the O-RCNN framework [2].

C. Quantitative Results

1) *Performance on DOTA-v1.0*: The proposed LEGNet achieves SOTA performance on the DOTA-v1.0 benchmark under single-scale evaluation. As shown in Table II, when LEGNet-S was equipped with the two-stage decoder O-RCNN [2], it achieved 80.03% mean average precision (mAP) with only 29.8M parameters, surpassing all existing one-stage and two-stage methods while maintaining competitive model complexity. Meanwhile, when it employed a single-stage decoder S²ANet [8], LEGNet-S consisted of 23.9M parameters and attained a mAP of 79.37%. Notably, LEGNet attains the best results in 12 out of 15 categories.

Compared with other efficient models, LEGNet-T establishes a new efficiency-accuracy trade-off, reaching 78.96%

mAP with merely 20.6M parameters - the lightest configuration among all listed methods. This represents a 0.92% mAP improvement over the previous efficient baseline (DecoupleNet-D2 [20]) while using 11.6% fewer parameters.

Our method particularly excels in detecting challenging categories (low-quality): (1) For small vehicles (SV), LEGNet-S achieves 81.42% AP, outperforming the previous best (PKINet-S [4]) by 0.61%; (2) In swimming pool (SP) detection, we obtain 82.00% AP, surpassing all competitors by at least 1.8%. (3) In helicopters (HC) detection, LEGNet-T achieves 71.39% AP, outperforming the PKINet-S [4] by 8.45% while using 33.1% fewer parameters. The results verify that LEGNet effectively balances parameter efficiency and detection accuracy across various oriented object categories, demonstrating superior generalization capability compared to existing Transformer-based and CNN-based approaches. To the best of our knowledge, these results represented the first instance of achieving a mAP exceeding 80% on the DOTA-v1.0 test set with single-scale training and testing protocol, marking a significant breakthrough in RSOD tasks. These findings underscored the critical importance of enhancing and extracting features from low-quality objects, which provided new avenues for follow-up research.

As presented in Table III, the effectiveness of LEGNet as a general-purpose backbone is further validated through comprehensive framework compatibility experiments. When integrated with various mainstream detection frameworks, our LEGNet-S consistently outperforms both ResNet-50 [38] and

TABLE III: Comparison of mAP with various decoders on DOTA-v1.0 test set under single-scale training and testing.

Framework		mAP (%) \uparrow		
		ResNet-50 [38]	PKINet-S [4]	LEGNet-S
One Stage	R-FCOS [45]	72.45	74.86	76.89
	R ³ Det [9]	69.70	75.89	77.62
	S ² ANet [8]	74.12	77.83	79.37
Two Stage	FR-O [43]	73.17	76.45	77.19
	Roi Trans. [7]	74.05	77.17	79.62
	O-RCNN [2]	75.87	78.39	80.03

the recent PKINet-S [4] across all architectural paradigms.

For single-stage detectors, LEGNet-S achieves significant improvements of +4.44% (R-FCOS [45]), +7.92% (R³Det [9]), and +5.25% (S²ANet [8]) in mAP over the original ResNet-50 implementations. When combined with the S²ANet framework, our backbone elevates the detection performance to 79.37% mAP.

In two-stage detectors, LEGNet-S demonstrates superior generalization capability with mAP gains of +5.57% for RoI Transformer [7] and +4.16% for O-RCNN [2] compared to their ResNet-50 counterparts. Particularly, the O-RCNN framework equipped with LEGNet-S reaches a new SOTA, outperforming its PKINet-S by 1.64% while maintaining comparable parameter efficiency.

These comprehensive comparisons confirm that LEGNet significantly enhances feature representation across various detection paradigms, achieving the most substantial improvements in complex scenarios. The consistent performance gains verify our architecture’s superior compatibility and learning capacity compared to existing backbone networks.

Table IV systematically evaluates the effectiveness of LEGNet as a backbone network when integrated with the O-RCNN [2] detection framework. Our LEGNet-S achieves SOTA performance with 80.03% mAP, surpassing all compared backbones while maintaining moderate computational complexity (12.7M parameters and 65.4G FLOPs). Notably, this represents a 4.16% mAP improvement over the baseline ResNet-50 backbone with 45.5% fewer parameters and 24.0% lower FLOPs.

The compact variant LEGNet-T demonstrates a superior efficiency-accuracy trade-off, attaining 78.96% mAP with only 3.6M parameters - 41.9% fewer than the previous most efficient competitor (DecoupleNet-D2 [20]) while delivering 0.92% higher mAP. Compared to recent advanced backbones, LEGNet-T outperforms PKINet-S by 0.57% mAP despite requiring 73.7% fewer parameters and 42.7% less computation.

Our architecture achieves the largest performance leap among all backbone upgrades for O-RCNN, and establishes new efficiency benchmarks, reducing backbone parameters by 84.5% compared to ResNet-50 while maintaining competitive detection accuracy. These findings confirm that LEGNet effectively addresses the critical challenge of balancing representation capacity and computational efficiency in RSOD tasks.

Table V compared the FPS of LEGNet with SOTA backbones. LEGNet-S achieves the highest mAP (80.03%) on DOTA 1.0 with O-RCNN detector, while maintaining competitive FPS (20.9) that is 1.77 \times faster than ARC-R50 [19]. This demonstrates its optimal trade-off between accuracy and

TABLE IV: Comparison of mAP with various backbones using O-RCNN [2] decoder on DOTA-v1.0 test set.

Backbone	Pub. Year	Backbone only		mAP (%) \uparrow
		#P \downarrow	FLOPs \downarrow	
ResNet-18 [38]	CVPR16	11.2M	38.1G	74.20
ResNet-50 [38]	CVPR16	23.3M	86.1G	75.87
ARC-R50 [19]	ICCV23	-	-	77.35
LSKNet-S [3]	ICCV23	14.4M	54.4G	77.49
DecoupleNet-D2 [20]	TGRS24	6.2M	23.1G	78.04
PKINet-S [4]	CVPR24	13.7M	70.2G	78.39
LEGNet-T	-	3.6M	30.2G	78.96
LEGNet-S	-	12.7M	65.4G	80.03

TABLE V: FPS comparison of various backbones using O-RCNN detector on DOTA 1.0 test set. All experiments were conducted on a single RTX 3090 GPU.

Methods	ARC-R50 [19]	LSKNet-S [3]	PKINet-S [4]	LEGNet-S
FPS \uparrow	11.8	22.5	5.4	20.9
mAP \uparrow	77.35	77.49	78.39	80.03

efficiency, enabled by lightweight architecture and adaptive feature enhancement, which is critical for real-time aerial image analysis in resource-constrained scenarios.

2) **Performance on DOTA-v1.5:** As shown in Table VI, the experimental results on the DOTA 1.5 test set demonstrate the superior performance of our proposed LEGNet-S compared to SOTA methods under single-scale training and testing protocols. LEGNet-S achieves the highest mAP of 72.89%, surpassing previous best-performing methods PKINet-S (71.47%) and SOOD [46] (70.39%) by 1.42% and 2.5%, respectively. Notably, our method attains 13 out of 16 category-wise highest and second highest AP values, including critical categories such as large vehicle (LV: 82.16% vs. 77.45%), ship(SH: 89.11% vs. 88.38%), roundabout (RA: 74.16% vs. 73.72%), and container crane (CC: 43.75% vs. 42.19%). Significant improvements are observed in other categories, where LEGNet-S outperforms existing methods by 0.03–4.65% margins. The results highlight robust generalization across diverse object scales and orientations, evidenced by consistent advantages in both small and large object categories.

3) **Performance on FAIRIM-v1.0:** The comparative evaluation on the FAIRIM-v1.0 benchmark further validates the effectiveness of LEGNet-S, as illustrated in Table VII. Our method achieves a SOTA mAP of 48.35%, outperforming existing approaches by 0.48% over the previous best-performing LSKNet-S (47.87%) and demonstrating 3.06% absolute improvement compared to the O-RCNN baseline (45.60%). Notably, LEGNet-S establishes consistent performance advantages across multiple architectural paradigms, including a 16.23% margin over anchor-free methods like Gliding Vertex [10] (29.92%) and 13.06% improvement relative to RoI Transformer [7] detectors (35.29%). These improvements substantiate the effectiveness of our architectural innovations in feature representation learning for RSOD tasks.

4) **Performance on DIOR-R:** The experimental results on the DIOR-R test set demonstrate the superior efficiency and accuracy of LEGNet-S framework. As summarized in Table VIII, LEGNet-S achieves SOTA detection performance with 68.40% mAP while maintaining the lowest model com-

TABLE VI: Experimental results on DOTA 1.5 test set [1] compared with SOTA methods with single-scale training and testing. LEGNet-S is built within O-RCNN [2] decoder. Other experimental results were referenced from PKINet [4] and SOOD [46].

Method	PL	BD	BR	GTF	SV	LV	SH	TC	BC	ST	SBF	RA	HA	SP	HC	CC	mAP \uparrow
RetinaNet-O [47]	71.43	77.64	42.12	64.65	44.53	56.79	73.31	90.84	76.02	59.96	46.95	69.24	59.65	64.52	48.06	0.83	59.16
FR-O [43]	71.89	74.47	44.45	59.87	51.28	68.98	79.37	90.78	77.38	67.50	47.75	69.72	61.22	65.28	60.47	1.54	62.00
Mask R-CNN [48]	76.84	73.51	49.90	57.80	51.31	71.34	79.75	90.46	74.21	66.07	46.21	70.61	63.07	64.46	57.81	9.42	62.67
HTC [49]	77.80	73.67	51.40	63.99	51.54	73.31	80.31	90.48	75.12	67.34	48.51	70.63	64.84	64.48	55.87	5.15	63.40
ReDet [44]	79.20	82.81	51.92	71.41	52.38	75.73	80.92	90.83	75.81	68.64	49.29	72.03	73.36	70.55	63.33	11.53	66.86
FSDet [50]	80.81	81.22	51.35	72.89	54.53	74.12	81.07	90.81	78.40	76.85	52.81	70.42	73.73	71.89	68.45	14.67	68.37
LSKNet-S [3]	72.05	84.94	55.41	74.93	52.42	77.45	81.17	90.85	79.44	69.00	62.10	73.72	77.49	75.29	55.81	42.19	70.26
SOOD [46]	80.32	84.41	52.59	74.77	58.48	76.90	86.97	90.87	78.62	76.56	62.93	71.16	74.64	76.04	55.97	25.09	70.39
PKINet-S [4]	80.31	85.00	55.61	74.38	52.41	76.85	88.38	90.87	79.04	68.78	67.47	72.45	76.24	74.53	64.07	37.13	71.47
LEGNet-S (ours)	80.48	85.04	55.64	74.86	52.64	82.16	89.11	90.88	84.55	68.91	66.21	74.16	77.44	74.68	65.76	43.75	72.89

TABLE VII: Comparison with SOTA methods on FAIR1M-v1.0. Other experimental results were referenced from LSKNet [3].

Method	G. V. [10]	RetinaNet [47]	C-RCNN [51]	FR-O [43]	RoI Trans. [7]	O-RCNN [2]	LSKNet-S [3]	LEGNet-S
mAP(%) \uparrow	29.92	30.67	31.18	32.12	35.29	45.60	47.87	48.35

TABLE VIII: Experimental results on DIOR-R test set [29]. Complexities were tested by 800 \times 800.

Method	#P \downarrow	FLOPs \downarrow	mAP (%) \uparrow
RetinaNet-O [47]	31.9	126.4	57.55
FR-O [43]	41.1	134.4	59.54
G.V. [10]	41.1	134.4	60.06
RoI Trans. [7]	55.1	148.4	63.87
LSKNet-S [3]	31.0	173.6	65.90
GGHL [52]	-	-	66.48
Oriented Rep [11]	36.6	118.8	66.71
DCFL [53]	36.1	-	66.80
PKINet-S [4]	30.8	118.1	67.03
LEGNet-S	29.9	118.1	68.40

plexity among compared methods, requiring only 29.9M parameters and 118.1G FLOPs. Our method delivers a 1.37% absolute mAP improvement over the previous best-performing PKINet-S (67.03%) while simultaneously reducing parameter counts by 0.9M (2.9% reduction). LEGNet-S achieves these advancements with equivalent computational costs to PKINet-S (118.1G FLOPs), outperforming all efficiency-oriented approaches including Oriented Rep [11] (66.71% mAP/118.8G FLOPs) and LSKNet-S (65.90% mAP/173.6G FLOPs). These advancements highlight LEGNet-S’s capability to effectively reconcile the accuracy-efficiency dilemma in oriented object detection, particularly beneficial for resource-constrained aerial image analysis scenarios.

5) **Performance on VisDrone2019:** The experimental results on the VisDrone2019 benchmark further substantiate the effectiveness of our proposed LEGNet-S framework, as detailed in Table IX. Integrated with the BAFNet [54] decoder, LEGNet-S establishes new SOTA performance across all evaluation metrics, achieving 32.2% AP - a 1.4% absolute improvement over the current best method BAFNet (30.8% AP). Our method exhibits particularly strong performance in small object detection (AP_s), achieving an AP of 24.5%, outperforming BAFNet by 2.1% and showing 10.2% and 10.7% relative improvements over GFL V1 [55] (14.3%) and DINO [58] (17.5%), respectively. LEGNet-S achieves 55.0% AP_{50} and 32.8% AP_{75} , surpassing BAFNet by 2.4% and 1.9%, respectively, indicating superior localization accuracy at multiple IoU thresholds. The framework maintains performance advantages across all object scales, particularly excelling in

TABLE IX: Results of LEGNet compared with SOTA methods on VisDrone2019 dataset [31]. LEGNet-S is built within BAFNet [54] decoder, and other experimental results were referenced from BAFNet.

Method	Pub. Year	AP	AP_{50}	AP_{75}	AP_s	AP_m	AP_l
GFL V1 [55]	NeurIPS20	23.4	38.2	24.2	14.3	34.7	40.1
CMDNet [56]	ICCVW21	29.2	49.5	29.8	16.1	35.9	36.5
QueryDet [57]	CVPR22	28.3	48.1	28.7	-	-	-
DINO [58]	ICLR23	26.8	44.2	28.9	17.5	37.3	41.3
RT-DETR [59]	CVPR24	15.9	36.5	10.7	13.8	28.4	23.1
BAFNet [54]	TGRS25	30.8	52.6	30.9	22.4	41.0	43.2
LEGNet-S	-	32.2	55.0	32.8	24.5	42.5	45.0

small object detection while significantly improving large object recognition (45.0% AP_l vs. BAFNet’s 43.2%). Compared with methods spanning 2020-2025, LEGNet-S shows 3.0% AP improvement over the 2023 DINO baseline and 16.3% gain compared to 2024’s RT-DETR [59], highlighting consistent performance evolution.

These results validate the enhanced feature representation capabilities of LEGNet-S when integrated with boundary-aware decoders, demonstrating particular effectiveness in handling drone-captured scenarios characterized by dense small objects and complex backgrounds.

D. Qualitative Results

The visual results on the DOTA-v1.0 test set were shown in Fig. 5. We conducted a visual analysis using SOTA backbones, including ARC-R50 [19] and PKINet [4], both of which were designed specifically for RSOD tasks. As depicted in Figure 5, LEGNet excelled at distinguishing blurry and low-quality objects, successfully detecting challenging low-quality objects such as ships, swimming pools, and small vehicles. In contrast, ResNet-50, ARC-R50, and PKINet demonstrated suboptimal performance when faced with the complexities of blurry or low-quality images in a single frame. Additionally, ResNet-50, ARC-R50, and PKINet exhibited false detections, mistaking clearly visible objects—such as a white object on the shore—for a ship, highlighting their limitations in boundary sensing.

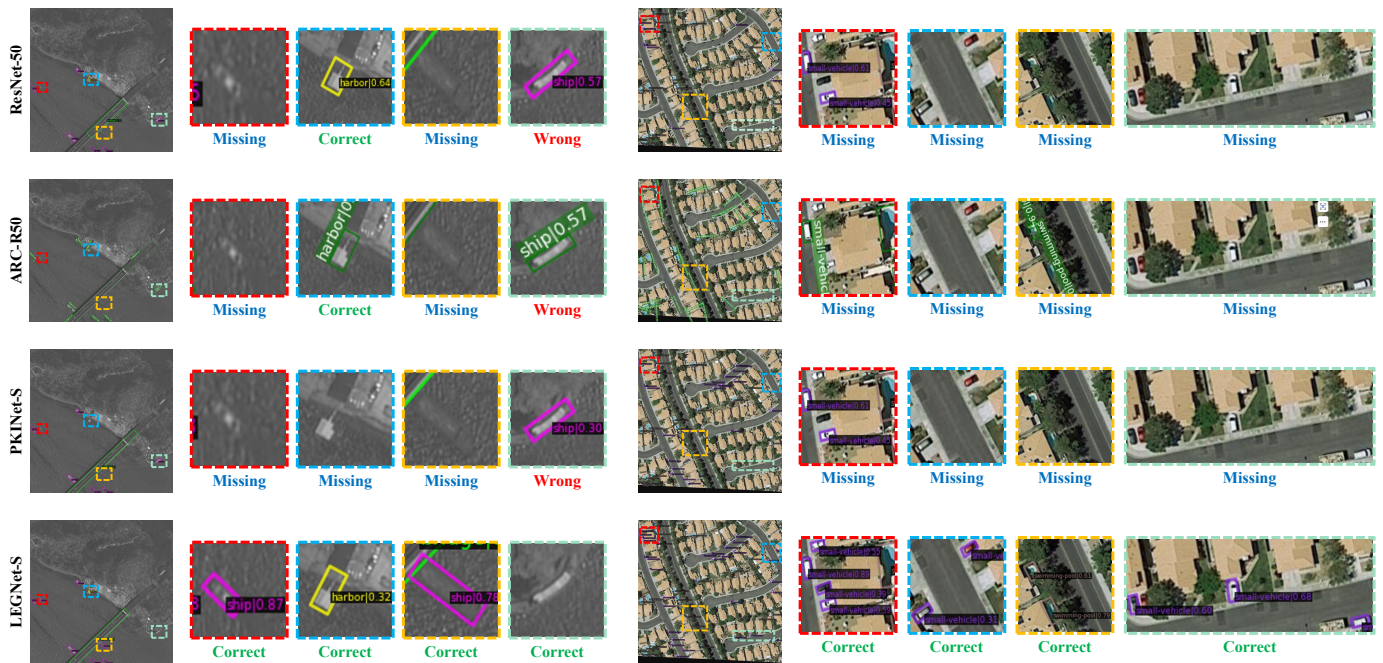


Fig. 5: Visualization of detection results on DOTA-v1.0 test set [1]. Input images resolution were 1024×1024 .

TABLE X: Ablation study of LEGNet on DOTA-v1.0 val set. Models was pre-train 100 epoch on Imagenet-1k.

LoG- -Stem	EGA	#P ↓	FLOPs ↓	mAP ↑	AP for each category (%) ↑			
					SV	LV	SP	HC
✓		20.61	135.6	70.8	59.7	84.0	55.3	46.0
		20.65	148.5	71.2	61.5	84.8	61.3	52.7
	✓	20.61	135.6	71.5	59.7	84.5	57.2	61.4
	LEGNet-T	20.65	148.5	72.2	63.2	85.0	59.6	58.3

E. Ablation Studies

Table X presented an ablation study of the proposed LEGNet method on the DOTA-v1.0 validation set, where various configurations were evaluated. We adopted a backbone with a 100-epoch pre-training schedule on the ImageNet-1K [33] for experimental efficiency, similar to [3], [4]. Experiments compared LEGNet-T with and without the LoG-Stem and EGA modules, as well as the individual removal of each module, and the full LEGNet-T. In the version without EGA, fixed convolutional kernels for edge and Gaussian attention were replaced with learnable convolutional kernels. The variant without the LoG-Stem employed learnable convolutional kernels with a kernel size of 4 and a stride of 4. The results reported the mAP for categories prone to low-quality or blurred challenges, such as small vehicles (SV), large vehicles (LV), swimming pools (SP), and helicopters (HC).

As shown in Table X, removing the EGA module slightly reduced the mAP to 71.2% compared to the full LEGNet-T (72.2%). The version without the LoG-Stem module showed a similar mAP (71.5%), but with a notable improvement in HC detection (61.4%) and a slight decline in other categories. LEGNet-T demonstrated the best overall performance, achieving the highest mAP of 72.2%, with significant improvements in SV detection (63.2%) and HC detection (58.3%). These results suggested that both the LoG-Stem and EGA modules

contributed to enhancing detection performance, especially for challenging categories.

F. Limitations and Future Works

The optimal kernel size for Gaussian attention should be selected cautiously, as its effectiveness likely varies across datasets with different object characteristics. Furthermore, although LEGNet outperforms current SOTA methods in RSOD tasks with fewer parameters and lower FLOPs, and includes non-gradient back-propagation Gaussian kernels that may improve efficiency, its FPS remains suboptimal. This is likely due to the underdeveloped optimizations compared to traditional convolution, which requires further investigation.

Future research may extend this framework to a broader range of downstream tasks such as semantic segmentation, instance segmentation, and object tracking. Leveraging the robust feature extraction and efficiency demonstrated in this work, these applications could significantly benefit from the integration of edge-Gaussian-driven modeling. Such an extension not only broadens the applicability of our approach but also opens up new avenues for achieving high performance in diverse computer vision challenges. We encourage future researchers to explore task-specific adaptations and to further optimize the framework in order to build versatile, scalable, and efficient systems that address real-world problems.

V. CONCLUSION

In this paper, we proposed LEGNet—a lightweight network designed for robust RSOD under low-quality imaging conditions. By integrating Scharr operator-based edge priors with uncertainty-aware Gaussian modeling, LEGNet enhances feature representation and object boundary clarity, achieving SOTA performance on multiple benchmarks while maintaining

computational efficiency. Overall, LEGNet bridges traditional image processing and deep learning, offering a promising balance between accuracy and efficiency. Future works could extend this framework to additional downstream tasks, providing a versatile foundation for further research in aerial and satellite image analysis.

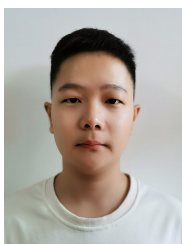
ACKNOWLEDGMENTS

This work was supported in part by NSFC Key Project of International (Regional) Cooperation and Exchanges (No. 61860206004), NSFC Key Project of Joint Fund for Enterprise Innovation and Development (No. U20B2068, U24A20342) and National Natural Science Foundation of China (No. 61976004).

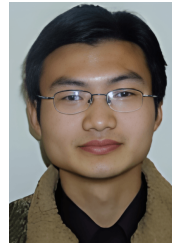
REFERENCES

- [1] G.-S. Xia, X. Bai, J. Ding, Z. Zhu, S. Belongie, J. Luo, M. Datcu, M. Pelillo, and L. Zhang, "Dota: A large-scale dataset for object detection in aerial images," in *Proc. IEEE Conf. Comput. Vis. Pattern Recog.*, 2018, pp. 3974–3983.
- [2] X. Xie, G. Cheng, J. Wang, X. Yao, and J. Han, "Oriented r-cnn for object detection," in *Proc. IEEE Conf. Int. Conf. Comput. Vis.*, 2021, pp. 3520–3529.
- [3] Y. Li, Q. Hou, Z. Zheng, M.-M. Cheng, J. Yang, and X. Li, "Large selective kernel network for remote sensing object detection," in *Proc. IEEE Conf. Int. Conf. Comput. Vis.*, 2023, pp. 16 794–16 805.
- [4] X. Cai, Q. Lai, Y. Wang, W. Wang, Z. Sun, and Y. Yao, "Poly kernel inception network for remote sensing detection," in *Proc. IEEE Conf. Comput. Vis. Pattern Recog.*, 2024, pp. 27 706–27 716.
- [5] X. Yang, H. Sun, K. Fu, J. Yang, X. Sun, M. Yan, and Z. Guo, "Automatic ship detection in remote sensing images from google earth of complex scenes based on multiscale rotation dense feature pyramid networks," *Remote Sens.*, vol. 10, no. 1, p. 132, 2018.
- [6] S. M. Azimi, E. Vig, R. Bahmanyar, M. Körner, and P. Reinartz, "Towards multi-class object detection in unconstrained remote sensing imagery," in *Proc. Asian Conf. Comput. Vis.*, 2018, pp. 150–165.
- [7] J. Ding, N. Xue, Y. Long, G.-S. Xia, and Q. Lu, "Learning roi transformer for oriented object detection in aerial images," in *Proc. IEEE Conf. Comput. Vis. Pattern Recog.*, 2019, pp. 2849–2858.
- [8] J. Han, J. Ding, J. Li, and G.-S. Xia, "Align deep features for oriented object detection," *IEEE Trans. Geosci. Remote Sens.*, vol. 60, pp. 1–11, 2021.
- [9] X. Yang, J. Yan, Z. Feng, and T. He, "R3det: Refined single-stage detector with feature refinement for rotating object," in *Proc. AAAI Conf. Artif. Intell.*, 2021, pp. 3163–3171.
- [10] Y. Xu, M. Fu, Q. Wang, Y. Wang, K. Chen, G.-S. Xia, and X. Bai, "Gliding vertex on the horizontal bounding box for multi-oriented object detection," *IEEE Trans. Pattern Anal. Mach. Intell.*, vol. 43, no. 4, pp. 1452–1459, 2020.
- [11] W. Li, Y. Chen, K. Hu, and J. Zhu, "Oriented reppoints for aerial object detection," in *Proc. IEEE Conf. Comput. Vis. Pattern Recog.*, 2022, pp. 1829–1838.
- [12] X. Yang and J. Yan, "Arbitrary-oriented object detection with circular smooth label," in *Proc. Eur. Conf. Comput. Vis.*, 2020, pp. 677–694.
- [13] X. Yang, J. Yang, J. Yan, Y. Zhang, T. Zhang, Z. Guo, X. Sun, and K. Fu, "Scrdet: Towards more robust detection for small, cluttered and rotated objects," in *Proc. IEEE Conf. Int. Conf. Comput. Vis.*, 2019, pp. 8232–8241.
- [14] X. Yang, J. Yan, Q. Ming, W. Wang, X. Zhang, and Q. Tian, "Rethinking rotated object detection with gaussian wasserstein distance loss," in *Proc. Int. Conf. Mach. Learn.*, 2021, pp. 11 830–11 841.
- [15] X. Yang, X. Yang, J. Yang, Q. Ming, W. Wang, Q. Tian, and J. Yan, "Learning high-precision bounding box for rotated object detection via kullback-leibler divergence," in *Proc. Adv. Neural Inform. Process. Syst.*, vol. 34, 2021, pp. 18 381–18 394.
- [16] X. Yang, Y. Zhou, G. Zhang, J. Yang, W. Wang, J. Yan, X. Zhang, and Q. Tian, "The KFIoU loss for rotated object detection," in *Proc. Int. Conf. Learn. Represent.*, 2023.
- [17] L. Dai, H. Liu, H. Tang, Z. Wu, and P. Song, "Ao2-DETR: Arbitrary-oriented object detection transformer," *IEEE Trans. Circuit Syst. Video Technol.*, vol. 33, no. 5, pp. 2342 – 2356, 2022.
- [18] Y. Tian, M. Zhang, J. Li, Y. Li, H. Yang, and W. Li, "Fpnformer: Rethink the method of processing the rotation-invariance and rotation-equivariance on arbitrary-oriented object detection," *IEEE Trans. Geosci. Remote Sens.*, vol. 62, pp. 1–10, 2024.
- [19] Y. Pu, Y. Wang, Z. Xia, Y. Han, Y. Wang, W. Gan, Z. Wang, S. Song, and G. Huang, "Adaptive rotated convolution for rotated object detection," in *Proc. IEEE Conf. Int. Conf. Comput. Vis.*, 2023, pp. 6589–6600.
- [20] W. Lu, S.-B. Chen, Q.-L. Shu, J. Tang, and B. Luo, "Decouplenet: A lightweight backbone network with efficient feature decoupling for remote sensing visual tasks," *IEEE Trans. Geosci. Remote Sens.*, vol. 62, pp. 1–13, 2024.
- [21] W. Lu, S. Chen, C. H. Q. Ding, J. Tang, and B. Luo, "Lwganet: A lightweight group attention backbone for remote sensing visual tasks," *arXiv.org*, vol. abs/2501.10040, 2025.
- [22] Y. Zhao, H. Sun, and S. Wang, "Small object detection in medium-low-resolution remote sensing images based on degradation reconstruction," *Remote Sens.*, vol. 16, no. 14, p. 2645, 2024.
- [23] Y. Li, S. Mavromatis, F. Zhang, Z. Du, J. Sequeira, Z. Wang, X. Zhao, and R. Liu, "Single-image super-resolution for remote sensing images using a deep generative adversarial network with local and global attention mechanisms," *IEEE Trans. Geosci. Remote Sens.*, vol. 60, pp. 1–24, 2022.
- [24] S. Jia, Z. Wang, Q. Li, X. Jia, and M. Xu, "Multiattention generative adversarial network for remote sensing image super-resolution," *IEEE Trans. Geosci. Remote Sens.*, vol. 60, pp. 1–15, 2022.
- [25] X. Feng, W. Zhang, X. Su, and Z. Xu, "Optical remote sensing image denoising and super-resolution reconstructing using optimized generative network in wavelet transform domain," *Remote Sens.*, vol. 13, no. 9, p. 1858, 2021.
- [26] L. Hou, K. Lu, X. Yang, Y. Li, and J. Xue, "G-rep: Gaussian representation for arbitrary-oriented object detection detection," *Remote Sens.*, vol. 15, no. 3, p. 757, 2023.
- [27] W. Lu, S. Chen, J. Tang, C. H. Q. Ding, and B. Luo, "A robust feature downsampling module for remote-sensing visual tasks," *IEEE Trans. Geosci. Remote Sens.*, vol. 61, pp. 1–12, 2023.
- [28] Q. Wang, B. Wu, P. Zhu, P. Li, W. Zuo, and Q. Hu, "Eca-Net: Efficient channel attention for deep convolutional neural networks," in *Proc. IEEE Conf. Comput. Vis. Pattern Recog.*, 2020, pp. 11 531–11 539.
- [29] G. Cheng, J. Wang, K. Li, X. Xie, C. Lang, Y. Yao, and J. Han, "Anchor-free oriented proposal generator for object detection," *IEEE Trans. Geosci. Remote Sens.*, vol. 60, pp. 1–11, 2022.
- [30] X. Sun, P. Wang, Z. Yan, F. Xu, R. Wang, W. Diao, J. Chen, J. Li, Y. Feng, T. Xu *et al.*, "FAIRIM: A benchmark dataset for fine-grained object recognition in high-resolution remote sensing imagery," *ISPRS J. Photogramm. Remote Sens.*, vol. 184, pp. 116–130, 2022.
- [31] D. Du, P. Zhu, L. Wen, X. Bian, H. Lin, Q. Hu, T. Peng, J. Zheng, X. Wang, Y. Zhang *et al.*, "Visdrone-det2019: The vision meets drone object detection in image challenge results," in *Proc. IEEE Conf. Int. Conf. Comput. Vis. Worksh.*, 2019.
- [32] K. Li, G. Wan, G. Cheng, L. Meng, and J. Han, "Object detection in optical remote sensing images: A survey and a new benchmark," *ISPRS J. Photogramm. Remote Sens.*, vol. 159, pp. 296–307, 2020.
- [33] J. Deng, W. Dong, R. Socher, L.-J. Li, K. Li, and L. Fei-Fei, "Imagenet: A large-scale hierarchical image database," in *Proc. IEEE Conf. Comput. Vis. Pattern Recog.*, 2009, pp. 248–255.
- [34] I. Loshchilov, "Decoupled weight decay regularization," *arXiv preprint arXiv:1711.05101*, 2017.
- [35] I. Loshchilov and F. Hutter, "Sgdr: Stochastic gradient descent with warm restarts," *arXiv preprint arXiv:1608.03983*, 2016.
- [36] Y. Zhou, X. Yang, G. Zhang, J. Wang, Y. Liu, L. Hou, X. Jiang, X. Liu, J. Yan, C. Lyu *et al.*, "Mmrotate: A rotated object detection benchmark using pytorch," in *Proc. ACM Int. Conf. Multimedia*, 2022, pp. 7331–7334.
- [37] A. Paszke, S. Gross, F. Massa, A. Lerer, J. Bradbury, G. Chanan, T. Killeen, Z. Lin, N. Gimelshein, L. Antiga *et al.*, "Pytorch: An imperative style, high-performance deep learning library," in *Proc. Adv. Neural Inform. Process. Syst.*, vol. 32, 2019.
- [38] K. He, X. Zhang, S. Ren, and J. Sun, "Deep residual learning for image recognition," in *Proc. IEEE Conf. Comput. Vis. Pattern Recog.*, 2016, pp. 770–778.
- [39] T. Ma, M. Mao, H. Zheng, P. Gao, X. Wang, S. Han, E. Ding, B. Zhang, and D. S. Doermann, "Oriented object detection with transformer," *arXiv*, vol. abs/2106.03146, 2021.
- [40] Y. Zeng, Y. Chen, X. Yang, Q. Li, and J. Yan, "ARS-DETR: Aspect ratio-sensitive detection transformer for aerial oriented object detection," *IEEE Trans. Geosci. Remote Sens.*, vol. 62, pp. 1–15, 2024.

- [41] L. Hou, K. Lu, J. Xue, and Y. Li, "Shape-adaptive selection and measurement for oriented object detection," in *Proc. AAAI Conf. Artif. Intell.*, 2022, pp. 923–932.
- [42] Y. Long, G.-S. Xia, S. Li, W. Yang, M. Y. Yang, X. X. Zhu, L. Zhang, and D. Li, "On creating benchmark dataset for aerial image interpretation: Reviews, guidances, and million-aid," *IEEE J. Sel. Topics Appl. Earth Observ. Remote Sens.*, vol. 14, pp. 4205–4230, 2021.
- [43] S. Ren, K. He, R. Girshick, and J. Sun, "Faster r-cnn: Towards real-time object detection with region proposal networks," *IEEE Trans. Pattern Anal. Mach. Intell.*, vol. 39, no. 6, pp. 1137–1149, 2016.
- [44] J. Han, J. Ding, N. Xue, and G.-S. Xia, "Redet: A rotation-equivariant detector for aerial object detection," in *Proc. IEEE Conf. Comput. Vis. Pattern Recog.*, 2021, pp. 2786–2795.
- [45] Z. Tian, C. Shen, H. Chen, and T. He, "Fcos: A simple and strong anchor-free object detector," *IEEE Trans. Pattern Anal. Mach. Intell.*, vol. 44, no. 4, pp. 1922–1933, 2020.
- [46] Y. Xi, T. Lu, X. Kang, and S. Li, "Structure-adaptive oriented object detection network for remote sensing images," *IEEE Trans. Geosci. Remote Sens.*, 2024.
- [47] T.-Y. Lin, P. Goyal, R. Girshick, K. He, and P. Dollár, "Focal loss for dense object detection," in *Proc. IEEE Conf. Int. Conf. Comput. Vis.*, 2017, pp. 2980–2988.
- [48] K. He, G. Gkioxari, P. Dollár, and R. Girshick, "Mask R-CNN," in *Proc. IEEE Conf. Int. Conf. Comput. Vis.*, 2017, pp. 2961–2969.
- [49] K. Chen, J. Pang, J. Wang, Y. Xiong, X. Li, S. Sun, W. Feng, Z. Liu, J. Shi, W. Ouyang *et al.*, "Hybrid task cascade for instance segmentation," in *Proc. IEEE Conf. Comput. Vis. Pattern Recog.*, 2019, pp. 4974–4983.
- [50] Y. Yu, X. Yang, J. Li, and X. Gao, "Object detection for aerial images with feature enhancement and soft label assignment," *IEEE Trans. Geosci. Remote Sens.*, vol. 60, pp. 1–16, 2022.
- [51] Z. Cai and N. Vasconcelos, "Cascade R-CNN: Delving into high quality object detection," in *Proc. IEEE Conf. Comput. Vis. Pattern Recog.*, 2018, pp. 6154–6162.
- [52] Z. Huang, W. Li, X.-G. Xia, and R. Tao, "A general gaussian heatmap label assignment for arbitrary-oriented object detection," *IEEE Trans. Image Process.*, vol. 31, pp. 1895–1910, 2022.
- [53] C. Xu, J. Ding, J. Wang, W. Yang, H. Yu, L. Yu, and G.-S. Xia, "Dynamic coarse-to-fine learning for oriented tiny object detection," in *Proc. IEEE Conf. Comput. Vis. Pattern Recog.*, 2023, pp. 7318–7328.
- [54] J. Song, M. Zhou, J. Luo, H. Pu, Y. Feng, X. Wei, and W. Jia, "Boundary-aware feature fusion with dual-stream attention for remote sensing small object detection," *IEEE Trans. Geosci. Remote Sens.*, vol. 63, pp. 1–13, 2025.
- [55] X. Li, W. Wang, L. Wu, S. Chen, X. Hu, J. Li, J. Tang, and J. Yang, "Generalized focal loss: Learning qualified and distributed bounding boxes for dense object detection," in *Proc. Adv. Neural Inform. Process. Syst.*, vol. 33, 2020, pp. 21 002–21 012.
- [56] C. Duan, Z. Wei, C. Zhang, S. Qu, and H. Wang, "Coarse-grained density map guided object detection in aerial images," *Proc. IEEE Conf. Int. Conf. Comput. Vis. Worksh.*, pp. 2789–2798, 2021.
- [57] C. Yang, Z. Huang, and N. Wang, "Querydet: Cascaded sparse query for accelerating high-resolution small object detection," in *Proc. IEEE Conf. Comput. Vis. Pattern Recog.*, 2022, pp. 13 658–13 667.
- [58] H. Zhang, F. Li, S. Liu, L. Zhang, H. Su, J. Zhu, L. M. Ni, and H.-Y. Shum, "Dino: Detr with improved denoising anchor boxes for end-to-end object detection," in *Proc. Int. Conf. Learn. Represent.*, 2023.
- [59] Y. Zhao, W. Lv, S. Xu, J. Wei, G. Wang, Q. Dang, Y. Liu, and J. Chen, "Detr beat yolos on real-time object detection," *Proc. IEEE Conf. Comput. Vis. Pattern Recog.*, pp. 16965–16974, 2024.



Wei Lu received the B.Eng. degree from Fuyang Normal University, China in 2020. He is currently pursuing a Ph.D. in computer science from Anhui University, Hefei, China. His current research interests include image processing, efficient AI, low-level visual tasks, and remote sensing. Many of his works have been accepted by top journals.



Si-Bao Chen received the B.S. and M.S. degrees in probability and statistics and the Ph.D. degree in computer science from Anhui University of China in 2000, 2003, and 2006, respectively. From 2006 to 2008, he was a Postdoctoral Researcher at the University of Science and Technology of China. Since 2008, he has been a teacher at Anhui University. From 2014 to 2015, he was a visiting scholar at the University of Texas in Arlington. His current research interests include image processing, pattern recognition, machine learning and computer vision.



Hui-Dong Li received the B.S. degree from Anhui University of Technology, Ma'anshan, China, in 2022. He is currently pursuing the M.S. degree in computer science and technology from Anhui University, Hefei, China. His research interests include object detection and remote sensing.



Qing-Ling Shu received the B.S. degree in computer science and technology from Anhui Normal University, Wuhu, China, in 2022. She is currently working toward the Ph.D. degree in computer technology from Anhui University of China. Her research interests include machine learning, pattern recognition, computer vision, and change detection in remote sensing.



Chris H.Q. Ding obtained his Ph.D. from Columbia University in 1987. He has held positions at the California Institute of Technology, Jet Propulsion Laboratory, Lawrence Berkeley National Laboratory, University of California, and the University of Texas in Arlington. Since 2021, he has been affiliated with the Chinese University of Hong Kong, Shenzhen. Dr. Ding is an expert in machine learning, data mining, bioinformatics, information retrieval, web link analysis, and high-performance computing. His works were cited over 60,000 times (Google scholar).



Jin Tang received the B.Eng. degree in automation and the Ph.D. degree in computer science from Anhui University, Hefei, China, in 1999 and 2007, respectively. He is currently a Professor with the School of Computer Science and Technology, Anhui University. His current research interests include computer vision, pattern recognition, machine learning, and deep learning. His works were cited nearly 10,000 times (Google scholar).



Bin Luo received the B.Eng. degree in electronics and the M.Eng. degree in computer science from Anhui University, Hefei, China, in 1984 and 1991, respectively, and the Ph.D. degree in computer science from the University of York, York, U.K., in 2002. From 2000 to 2004, he was a Research Associate with the University of York. He is currently a Professor with Anhui University. His current research interests include graph spectral analysis, image and graph matching, statistical pattern recognition, digital watermarking, and information security. His works were cited over 10,000 times (Google scholar).